

Influence of Strong Spatially Varying Near Fault Ground Motion on Steel Box Arch Bridge

Zhen Liu (✉ 201913693@sdtbu.edu.cn)

Shandong Technology and Business University <https://orcid.org/0000-0001-8317-1355>

Shibo Zhang

Shandong Technology and Business University

Research Article

Keywords: strong spatially varying, near fault ground motion, steel box arch bridge, shaking table experiment

Posted Date: May 19th, 2021

DOI: <https://doi.org/10.21203/rs.3.rs-272843/v1>

License: © ⓘ This work is licensed under a Creative Commons Attribution 4.0 International License. [Read Full License](#)

Version of Record: A version of this preprint was published at Bulletin of Earthquake Engineering on July 27th, 2021. See the published version at <https://doi.org/10.1007/s10518-021-01182-1>.

Abstract

In violent earthquakes, ground motion is considered to change dramatically in the process of spatial propagation. Strong spatially varying exists in ground motion near fault area, and it can cause the large-span and large stiffness structure to be damaged. In this paper, a typical long-span steel box arch bridge is selected as an engineering case. In order to simulate the spatially varying of near fault ground motion accurately, the records that sampled in former earthquake are used as ground motion input. The shaking table experiment and finite element analysis are used as analysis means. Through the analysis of the internal force and displacement response of the key position of the arch rib, it is found that the spatially varying in the near fault ground motion can bring severe seismic response. If the spatially varying is ignored, the damage of the bridge will be seriously underestimated.

1. Introduction

Near fault ground motions are believed to contain large amounts of energy and have strong spatially varying characteristics.(Ellsworth et al. 2013; Fang, Cheng, *et al.* 2018; Abdollahzadeh, G., *et al.*2018). It has been proved that the earthquake in the near fault area can bring more damage to structures than others(Guo W, *et al.*2020;Zhong, J., *et al.*2020; Zhang, C. et al. 2020; Pan, X. *et al.*2017). A steel box arch bridge is usually used in lifeline traffic and plays an important role because of its beautiful appearance, long span, and good economic indicators. Some lifeline traffic are difficult to completely avoid faults due to the factors of construction site and route selection, which makes some long-span steel box arch bridges inevitably affected by faults (Goel and Anil 2008;Goel, Rakesh, *et al.* 2014).The steel box arch bridges with large span are more vulnerable to the permanent displacement of the fault area. Due to the large stiffness, they are very sensitive to the temporary displacement in the near fault area. Once these steel box arch bridges are damaged, the regional traffic will be cut off and the disaster relief work will be seriously affected.

In this paper, the damage of steel box arch bridge under strong spatially varying near fault ground motions is studied. The occurrence of this kind of earthquake damage needs two necessary conditions. First, the energy released by the earthquake is high, and the variation of ground motion near fault is strong. Second, the long-span steel box arch bridge is located in the near fault area. Due to these above limitations, there were few cases of earthquake damage. However, due to the huge damage of strong spatially varying near fault ground motion and the sensitivity of steel box arch bridge to this kind of earthquake, once it occurs, the bridge will be seriously damaged. For example, during the Kobe earthquake in 1995, there were four steel box arch bridges in the near fault area, two of them were seriously damaged, one was slightly damaged. For the Nishinomiya port bridge with a main span of 252 meters, the superstructure of the bridge dropped due to the excessive displacement of the substructure. For the Rokko island Bridge with a main span of 217 meters, the steel bearing falls off and the wind brace yields(Wilson 2003). From these earthquake damage cases, it can be found that once strong earthquake occurs in the near fault area, the steel box arch bridge within the region will be seriously damaged. In the case of Kobe earthquake, the damage rate of four steel box arch bridges in the near fault area reached 75%, and the failure rate reached 50%.

At present, there is a serious underestimate of the strong spatially varying in the near fault, which results in the underestimate of structural damage, especially for the large span and stiffness structure such as steel box arch bridge. Generally, the time interval method takes the spatially varying into account, it simulates the different vibration of each excitation point through time interval, then to simulates the spatially varying of the ground motion. This method is very classical, which has been used in the seismic designs of many long-span bridges (Mehannyet al. 2014;Zhao 2013). In essence, the ground motion of each excitation point is assumed to be exactly the same by this time interval method, and there are only differences in the starting time of excitation. This simplification is effective for the far-field ground motion with gentle change, but for the near-field ground motion with severe change the seismic impact is obviously underestimated.

For this reason, many methods have been used to study the damage of long-span and large stiffness structures due to the strong spatially varying in the near fault area. In some methods, the strong spatially varying earthquake motion under complex conditions is regarded as the superposition of different frequency signals, so the signal analysis techniques such as wavelet technology and empirical mode decomposition are used for analysis and synthesis, and for further analysis of the long-span bridges(Konakli and Armen 2012;Dinh *et al.*2014). In other methods, evolution spectrum, random vibration theory, dynamic increment analysis and other seismic damage analysis methods are directly used to study the damage of long-span structures under strong spatially varying near fault ground motion(Mehannyet al. 2014.;Adanuret al. 2016, Cao, Yenan, *et al.* 2017). The long-span structures under strong spatially varying near fault ground motion are analyzed in detail by these methods. In recent years, the most advanced signal analysis techniques are used in seismic damage analysis. However, they are still difficult to predict the strong spatially varying in the near fault area, which makes the damage more difficult to analyze.

In this paper, another method is used to analyze the damage of steel box arch bridge under the strong spatially varying near fault ground motion. The actual records of the near fault ground motion with strong spatially varying effect is selected as input load, under which the damage of steel box arch bridge is analyzed by finite element analysis program and shaking table test. Thus, the intensity of the spatially varying of the real near fault area is revealed, and the damage of the spatially varying to the long-span steel box arch bridge is analyzed.

2. Bridge Case

The case of steel box arch bridge used in this paper is the Datengxia bridge in Yunnan province, China. The author participated in its design. The main bridge is 230m long and 12m wide, which is about 1.9km downstream of the Datengxia water control project. The overview of the bridge is shown in Fig. 1. The bridge location is particularly important, connecting many traffic lines on both sides. And there is a main waterway under the bridge. Once the bridge is destroyed in earthquake, the cross-strait traffic lines will be cut off, and the safety of the whole water conservancy project will be affected.

The design fortification intensity of the bridge is VII degrees. There is one fault passing through, so the near fault effect is considered. The design load is determined as class I highway, and the design reference period is 100 years. The line shape of main arch axis is quadratic parabola. The main dimensions of the bridge are shown in Fig. 1 and the material parameters used are listed in Table 1.

Table 1
Material parameters

Material	Component	Compressive strength	Tensile strength	Elastic modulus	Density	Poisson's ratio
Q345	Main arch	345.0MPa	345.0MPa	206GPa	$7.8E3(\text{kg}\cdot\text{m}^{-3})$	0.3
C50	Main beam, cross beam bridge deck	50.0MPa	2.7MPa	35GPa	$2.5 E3(\text{kg}\cdot\text{m}^{-3})$	0.2

3. Shaking Table Experiment

Due to the long time-consuming, high cost, and many equipment requirements, shaking table test is not widely carried out in structure seismic analysis. However, the sample bridge has large span and large stiffness, which is easily affected by the non-uniform excitation of near fault ground motion, and then causes structural damage. In order to ensure the accuracy of seismic analysis, carried out for the case bridge. The non-uniform excitation was exerted, thus the possible damage of the case bridge under the action of near fault ground motion is simulated.

If the scaled model excited by the shaking table is made of the same material as the case structure, the entire process of elastic-plastic deformation and prediction of structural damage under various excitation conditions can be simulated accurately. However, it cannot be realized. The total weight of Datengxia bridge is 9600 ~ 10000 tons. Even with a small scale of 1 / 30, the total weight of the scaled model will be 10 tons, which exceeds the maximum load of the shaking table used in the test. Otherwise, with such small scale ratio, the thickness of the main arch of the structure is only 1mm. During the processing of 1 mm steel, large residual deformation and stress will be produced, which will affect the accuracy of the structure. After repeated comparison, plexiglass is selected as the material of the scaled model. The mechanical properties of plexiglass are stable and easy to manufacture. According to the equipment condition and the bridge size, the similarity ratio of main physical quantities is listed in Table 2.

Table 2
Model scale parameters

Physical quantity	Symbol	Dimension	Symbol of similar constant	Similarity constant
Length	L	L	S_L	2.86E-02
Mass	m	M	S_m	1.19E-05
Force	F	$MT^{-2}L$	S_F	1.19E-05
Stress	σ	$MT^{-2}L^{-1}$	S_σ	1.46E-02
Strain	ε	-	S_ε	1.00E + 00
Modulus of elasticity	E	$MT^{-2}L^{-1}$	S_E	1.46E-02
Density	ρ	ML^{-3}	S_ρ	5.12E-01
Frequency	ω	T^{-1}	S_ω	5.92E + 00
Acceleration	a	LT^{-2}	S_a	1.00E + 00
Velocity	v	LT^{-1}	S_v	1.69E-01
Time	t	T	S_t	1.69E-01

Due to the time scale ratio, the natural ground motion must be adjusted before it is input into the shaking table. For example, the original ground motion is shown in Figs. 2 (a) - (b). After the adjustment according to the time scale ratio of 1.6903e-01, new results can be seen in Figs. 2 (c) - (d). However, due to the condition of shaking table (the maximum excitation frequency is 20Hz), the signal higher than 20Hz cannot be input into the structure. In this paper, empirical mode decomposition(EMD) is used to decompose the ground motion, and then to remove the ground motion components higher than 20Hz. Finally, the acceleration time history of the actual input structure is shown in Figs. 2 (e) - (f). Although the signal higher than 20Hz is removed, 81.19% of the signal energy is input. If the cumulative square velocity (CSV) is used to represent the signal energy, 99.84% of the CSV is retained. In order to further analyze this deviation, the acceleration response spectrum of the original ground motion and the adjusted ground motion after removing the high frequency component are drawn as Fig. 3(the damping ratio is 0.03). According to Fig. 3, the difference between the two acceleration response spectra is not obvious. The main difference occurs below 0.1s, and the first five natural vibration periods of the case bridge are greater than 0.1s, so this input method will not bring too much error.

The main properties of model materials and actual engineering materials are listed in Table 3. As the main material of the bridge, parameters of Q345 steel are used in the calculation of similarity ratio. According to the elastic modulus, the concrete is converted into steel and then simulated by plexiglass. After the scaled model is made, the counterweight (Table 4) is used to supplement the mass difference. Because the size of the stiffener in the arch rib is too small, it can only be converted according to the principle of similar stiffness. The size of the arch rib model is shown in Fig. 4, and the final model is shown in the Fig. 5.

Table 3
Material parameters

Material	Compressive strength	Tensile strength	Elastic modulus	Poisson's ratio	Density
plexiglass	55.5MPa	67.2Mpa	3012Mpa	0.36	1.2E3(kg·m ⁻³)
Q345	345.0MPa	345.0MPa	206GPa	0.30	7.8E3(kg·m ⁻³)
C50	50.0MPa	2.7MPa	35GPa	0.2	2.5 E3(kg·m ⁻³)

Table.4 Counterweight parameter

Component	Real bridge(10 ³ kg)	Real bridge converted mass (kg)	Model actual mass(kg)	Counterweight(kg)
Arch rib	2006.287	23.941	6.500	17.441
Arch abutment	1262.952	15.071	2.045	13.026
Bridge suspender	46.400	0.554	0.256	0.298
Main beam	9337.470	111.424	18.681	92.743
Deck pavement	1117.050	13.330	0.000	13.330
Total	13770.159	164.319	27.482	136.837

Because the scaled model is made of plexiglass with low weight, the collection device should be arranged reasonably to reduce the influence on the test results. The physical quantities obtained in this test are the strain, acceleration and displacement of the model. For strain acquisition, the instrument is arranged at the arch foot, one-quarter arch rib on both sides, and the arch crown respectively(Fig. 6). For acceleration acquisition, due to the sensor in hand can only acquire one direction signal, so three acceleration sensors are combined to obtain three-direction signals at the same point(Figs. 7 (a)-(b)). Seven acceleration measuring points are arranged in the bridge. In order to improve the utilization, all measuring points are arranged on one No.1 arch rib of the bridge. For displacement acquisition, traditional cable displacement meter is not suitable for this model, only laser displacement meter can be used. A single laser displacement meter can only obtain the dynamic displacement in one direction. In this paper, two lasers are combined to obtain the two-direction displacement signal of one point(Figs. 7 (d)). The obtained acceleration signals and displacement signals can be checked each other. Laser displacement meter and acceleration sensor are arranged separately to improve acquisition efficiency. The laser displacement meter is arranged on the arch rib without acceleration sensor. The acquisition system is shown in Fig. 7 and the arrangement is shown in Fig. 6.

The shaking table used in this paper is a three-direction one. With closed-loop feedback control mechanism, the controller will reversely adjust the excitation of the shaking table according to the actual vibration of the shaking table, so that the actual vibration of the shaking table is consistent with the input signal. Specific parameters of the vibration table are listed in Table 5.

Table 5
Parameter of shaking table

Parameter	value
Freedom of motion	three directions
Shaking table size	1.5×1.5m
Shaking table load	1E4kg
Shaking table thrust	200kN
Shaking table frequency	0.1 ~ 20Hz
Shaking table acceleration	2g
Maximum velocity	330mm/s
Maximum displacement	300mm

4. Finite Element Simulation

According to the project overview, the finite element model is established by the finite element program ANSYS for seismic analysis. The accuracy and the complexity of the model should be taken into account when modeling to ensure that the relatively accurate results can be calculated in the shortest possible time. The 3-D beam element is used to simulate the main arch rib, wind support, longitudinal beam and cross beam. The link element is used to simulate suspender and tie bar. The deck system is regarded as the reinforcement of the longitudinal beam and the cross beam. The rigidity of the deck system is allocated to the longitudinal beam and the cross beam. The mass element is used to simulate the mass of deck system and attachment structure, and is added at the joint of suspender and beam. The steel box arch bridge case model is shown in Fig. 8.

The selection of constitutive relation will directly affect the accuracy of finite element calculation, especially for the time history analysis of earthquake. During a strong earthquake, the structure will enter the plastic stage. The low cycle fatigue of members will be caused by the reciprocating action of seismic force. In this model, the main arch is made of Q345 steel. The constitutive model of steel mainly includes ideal

elastic-plastic model, linear strengthening model and curve elastic-plastic strengthening model. Among the three models, the curve elastic-plastic strengthening model can reflect actual steel constitutive relationship best. However, considering that the model in this paper needs a lot of seismic time history analysis, in order to reduce the amount of calculation, the linear strengthening model is selected as the constitutive model of Q345 steel. The modulus of elasticity before and after yield is taken as 206GPa and 2.06GPa respectively. The yield strength is taken as 345MPa, then the yield strain is determined to be 1.68E-3. An appropriately large maximum strain of 0.01 is selected in consideration of safety. This constitutive relation is expressed by Eq. (1).

$$f_{\varepsilon} = \begin{cases} E_s \varepsilon & 0 \leq \varepsilon \leq \varepsilon_y \\ E_y \varepsilon & \varepsilon_y < \varepsilon \leq \varepsilon_{sh} \end{cases} \quad (1)$$

In Eq. (1), E_s and E_y represent the elastic modulus of Q345 steel before and after yield respectively. Correspondingly, ε_y and ε_{sh} represent yield strain and maximum strain.

Concrete is a mixture of sand, stone, water and cement in a certain proportion. When the concrete is stressed, there will be complex interaction between the components. Correspondingly, the stress-strain relationship is also very complex. After decades of experimental research, dozens of models have been used to describe the constitutive relationship of concrete. Most of them are considered to be too complex and have too many parameters. So they are not suitable for a large number of time history analysis. In this paper, the Hognestad model, which is widely used due to its simple form, is selected. The rising part of this model is a parabola and the falling part is a straight line, as shown in Eq. (2).

$$f_{\varepsilon} = \begin{cases} f_0 \left[2 \frac{\varepsilon}{\varepsilon_0} - \left(\frac{\varepsilon}{\varepsilon_0} \right)^2 \right] & 0 \leq \varepsilon \leq \varepsilon_0 \\ f_0 \left[1 - 0.15 \left(\frac{\varepsilon - \varepsilon_0}{\varepsilon_u - \varepsilon_0} \right) \right] & \varepsilon_0 < \varepsilon \leq \varepsilon_u \end{cases} \quad (2)$$

Because C50 concrete is used in this project, the peak stress (f_0) is taken as 50MPa, the peak strain ε_0 is taken as 0.0014, and the maximum compressive strain ε_u is taken as 0.0033. The density of steel and concrete is 7.85E3kg/m³ and 2.46E3kg/m³ respectively. The mass of deck system and ancillary structure is divided into mass blocks by length and added at the joints of longitudinal and transverse members. After repeated simulation, it is reasonable to take 50 tons as the weight of each concentrated mass block. In the model, the mass and stiffness that proportional to Rayleigh damping have been considered, and the modal damping ratio is 0.03, then Rayleigh damping parameters are calculated.

5. Modal Analysis

Based on the test and simulation, the two methods are comprehensively used to check and compare the seismic response of a bridge with large rigidity under strong spatially varying ground motion action. The seismic response of a bridge with large stiffness under strong spatially variable earthquake is systematically analyzed. After the scaled model and finite element model have been established, modal analysis is required. For the scaled model, the vibration mode is excited by inputting a pulse using the shaking table. For the finite element model, the vibration mode is obtained by using the block Lanczos method.

For the scaled model, the acceleration and displacement time histories of each sensor are analyzed, and then the frequency of each mode is obtained. The damping ratio collected by the instrument is listed in Table 6. Because it is difficult to obtain the higher order modes of the scaled model, only first five orders are shown in Table 6.

Table 6
Measured modes and frequencies

Mode order	Mode characteristics	Frequency /Hz	Damping ratio
1	Longitudinal floating main beam	1.29	0.023
2	Vertical first order anti symmetric bending of main arch and bridge deck	1.60	0.020
3	Vertical first-order symmetric bending of main arch and bridge deck	2.48	0.027
4	Vertical second order symmetric bending of main arch and bridge deck	3.26	0.016
5	Transverse anti symmetric bending of main arch and bridge deck	4.27	0.033

After obtaining these modes of scaled model, they are compared with the results of the finite element model to mutually check the accuracy. The first 9 modes frequencies (Table 7) and vibration modes (Fig. 9) of the model are obtained by using block Lanczos method in ANSYS.

Table 7
The first nine modes and frequencies of finite element method

Mode order	Mode characteristics	Frequency /Hz	Relative error (%)
1	Longitudinal floating main beam	1.36	5.50
2	Vertical first order anti symmetric bending of main arch and bridge deck	1.42	-11.23
3	Vertical first-order symmetric bending of main arch and bridge deck	2.15	-13.44
4	Vertical second order symmetric bending of main arch and bridge deck	3.04	-6.82
5	Transverse anti symmetric bending of main arch and bridge deck	3.57	-16.36
6	Vertical second order anti symmetric bending of main arch and bridge deck	4.32	
7	First order torsion of main arch and bridge deck	6.57	
8	Vertical third-order symmetric bending of main arch and bridge deck	6.86	
9	Second order torsion of main arch and bridge deck	10.34	

By analyzing the vibration modes and frequencies of each order, it can be found that the difference between the measured values of the scaled model and the calculated results of the finite element is little. Especially for the first three order vibration, the average error can be controlled lower than 10%. The little difference is difficult to eliminate due to the uncertainty in the process of the hand made scaled model. The adhesive used to make the model will have a small amount of cracking due to the change of humidity during the experiment. A few errors will also be brought in during the sampling of acceleration and displacement signals. However, the difference of 10% between the scaled model and the finite element model is considered to be within the acceptable range.

6. Ground Motion Samples

In this paper, the damage of long-span bridge caused by spatially varying effect in near fault earthquake is studied. Ground motion samples are required to reflect both spatially varying and near fault effects. In order to achieve these two purposes, the ground motion samples acquisition area should be as close to the fault as possible and the distance between the measuring points should be close. The earthquake records that meet the two conditions are very limited. After searching the Pacific Earthquake Engineering Research (PEER) Center database, the records measured in the Ms5.9 earthquake are selected as the ground motion samples. The Ms5.9 earthquake occurred in the offshore of Taiwan Island on January 29, 1981, records are collected by SMART1 seismic station. The relevant parameters of the measuring points are listed in Table 8, and the relative positions of the measuring points are drawn in Fig. 10.

Table 8
The relevant parameters of the measuring points

Ground motion number	Seismic station	$V30$ (ms^{-1})	Station coordinate		$PGA(g)$		
			$X(\text{km})$	$Y(\text{km})$	W-E	N-S	U-D
306	SMART1C00	309.41	27.15	-13.30	0.10	0.11	0.04
307	SMART1I06	309.41	26.96	-13.24	0.09	0.08	0.03
308	SMART1I12	275.82	27.34	-13.35	0.14	0.11	0.06
309	SMART1M01	268.37	28.08	-13.09	0.08	0.18	0.09
310	SMART1M07	327.61	26.16	-13.56	0.11	0.11	0.05
311	SMART1O01	267.67	29.19	-12.89	0.09	0.12	0.03
312	SMART1O07	314.33	25.11	-13.71	0.09	0.08	0.03
3559	SMART1I03	314.88	27.20	-13.11	0.08	0.09	0.05
3560	SMART1I09	309.41	27.10	-13.49	0.09	0.08	0.07
3561	SMART1M02	306.78	27.85	-12.65	0.12	0.12	0.05
3562	SMART1M03	306.78	27.43	-12.39	0.06	0.12	0.03
3563	SMART1M04	306.38	26.94	-12.37	0.16	0.13	0.03
3564	SMART1M05	306.38	26.50	-12.60	0.12	0.10	0.04
3565	SMART1M06	308.39	26.24	-13.02	0.06	0.10	0.05
3566	SMART1M08	301.05	26.45	-13.95	0.10	0.10	0.04
3567	SMART1M09	321.63	26.87	-14.21	0.07	0.07	0.03
3568	SMART1M10	321.63	27.36	-14.23	0.13	0.12	0.04
3570	SMART1M12	275.82	27.80	-14.00	0.10	0.15	0.05
3571	SMART1O02	285.09	28.71	-11.92	0.14	0.25	0.04
3572	SMART1O03	278.32	27.81	-11.33	0.16	0.13	0.03
3573	SMART1O04	288.24	26.74	-11.26	0.13	0.11	0.03
3574	SMART1O05	286.03	25.77	-11.74	0.10	0.12	0.02
3575	SMART1O06	293.46	25.18	-12.64	0.12	0.10	0.04
3576	SMART1O09	329.08	26.49	-15.27	0.12	0.09	0.04
3577	SMART1O10	320.11	27.56	-15.34	0.09	0.11	0.04
3578	SMART1O12	303.36	29.12	-13.96	0.09	0.16	0.03

It can be found from Table 8 that the distances between 306–307 and 306–308 are 195.3m and 198.2m respectively, which are shorter than the bridge length of 230m, and the site conditions and bridge location are also very similar. Therefore, these two groups of seismic records are used as the ground motion samples. These ground motion samples are shown in Figs. 11–13. The near fault velocity pulse recognition method based on wavelet is used to extract the near fault velocity pulse in these samples, as shown in Fig. 14.

7. Uniform excitation

In order to obtain the seismic response of the bridge under uniform excitation, the No. 306, 307 and 308 ground motions with near fault velocity pulse are input into the structure respectively. The north-south, east-west and vertical ground motion components in the sample are taken as the longitudinal, transverse and vertical excitations to input the model respectively. The data collected by the dynamic stress and displacement acquisition system are processed, and the seismic responses of the key positions such as arch foot, quarter arch rib and vault are obtained. The seismic response obtained from the shaking table experiment is compared with that from the finite element calculation, as

shown in Tables9-10. The time history of the displacement at the top of the arch rib (No.1 arch rib) and the internal force at the left arch foot are shown in Figs. 15–16.

Table 9
Displacement response of key nodes

Position	Result	No.1 Arch rib								
		2			3			4		
		Axial direction	Transverse direction	Vertical direction	Axial direction	Transverse direction	Vertical direction	Axial direction	Transverse direction	Vertical direction
306	Finite element	12.11	59.57	10.49	13.16	64.24	12.61	10.94	58.69	11.29
	Experiment	12.51	67.17	9.49	11.62	77.24	11.35	12.22	63.99	9.45
	Relative error	3.19%	11.32%	10.56%	13.32%	16.83%	11.09%	10.47%	8.29%	19.50%
307	Finite element	9.42	51.42	9.96	14.98	75.67	14.75	9.65	50.66	9.25
	Experiment	10.41	42.24	10.64	12.38	66.27	17.63	7.93	60.75	8.34
	Relative error	9.52%	21.75%	6.39%	21.01%	14.18%	16.32%	21.78%	16.60%	10.96%
308	Finite element	17.90	87.74	16.60	18.13	92.12	17.81	17.30	86.44	16.02
	Experiment	15.09	101.73	13.46	18.84	113.80	18.44	17.47	95.91	16.62
	Relative error	18.61%	13.75%	23.34%	3.75%	19.05%	3.44%	0.98%	9.87%	3.61%

Table 10
Axial force response of key nodes

Position	Result	No.1 Arch rib					No.2 Arch rib				
		1	2	3	4	5	1	2	3	4	5
306	Finite element	5670.00	2101.61	1500.67	2111.32	6164.16	5878.00	2125.82	1505.41	2398.62	6512.72
	Experiment	6454.98	2432.84	1911.39	2474.23	5069.21	4878.17	2136.23	1613.27	2839.00	8465.74
	Relative error	12.16%	13.62%	21.49%	14.67%	21.60%	20.50%	0.49%	6.69%	15.51%	23.07%
307	Finite element	4865.00	1622.56	1285.81	1918.72	5531.55	5124.00	2030.18	1412.81	1542.20	4384.85
	Experiment	5388.92	2042.73	1274.17	2233.13	4760.07	6543.78	2433.11	1696.27	1595.13	5268.98
	Relative error	9.72%	20.57%	0.91%	14.08%	16.21%	21.70%	16.56%	16.71%	3.32%	16.78%
308	Finite element	5621.55	2061.38	1447.80	1738.13	4549.88	4549.88	2322.62	1626.63	2525.14	4858.78
	Experiment	5209.44	2439.17	1582.30	2033.56	4066.05	4066.05	2494.40	2058.23	2763.28	5809.55
	Relative error	7.91%	15.49%	8.50%	14.53%	11.90%	11.90%	6.89%	20.97%	8.62%	16.37%

The following conclusions can be drawn by analyzing the above seismic responses: 1. The seismic damage of bridge can be controlled within slight degree. The maximum transverse displacement of the arch crown is 113.8mm and the maximum axial force is 8465.74kn, which may cause slight damage to the arch rib, but no serious damage or collapse. 2. The displacement response in the arch rib may be greatly affected by the acceleration in the ground motion excitation, while the axial force response in the arch rib may be greatly affected by the velocity pulse in the ground motion excitation. It can be found from Fig. 17 that the maximum transverse displacement of the arch crown has basically positive correlation with the maximum acceleration of transverse ground motion excitation, while there is no obvious correlation with the peak value of ground motion velocity pulse. Similarly, the average axial force of key nodes of the arch rib has basically positive correlation with peak value of ground motion velocity pulse. According to the limited samples, a conclusion can be drawn that the peak value of ground motion basically corresponds to the displacement response, while the velocity pulse corresponds to the internal force of arch rib. 3. The time point of the most severe earthquake response is generally lagging behind the peak value and velocity pulse of the ground motion excitation. By analyzing the comparison of seismic excitation and seismic response of key nodes(Fig. 18), the maximum value appears after the peak value

of the near-fault velocity pulse, which indicates that the seismic response of steel box arch bridge needs a period of time to accumulate excitation energy, and the accumulation time is about 2-3s for the bridge sample. 4. The relative difference of displacement is less than that of internal force. The average difference between the measured displacement value and the finite element calculation value is 12.57%, while the value of internal force is 14.36%. The difference is due to the fact that the measured values of internal forces need to be converted by dynamic strain collection system, while the measured values of displacements are obtained directly.

8. Non-uniform Excitation

In order to study the influence of spatial variation effect on the case bridge, 306 and 307 ground motions as well as 306 and 308 ground motions are paired. The excitation is input on both sides of the arch bridge, and then the direction of the excitation is adjusted according to Fig. 10. The input direction of ground motion excitation is shown in Fig. 19, the east-west and north-south components of the ground motion are adjusted to the longitudinal and transverse bridge components. Then the displacement difference between the two excitation points of the bridge can be obtained by comparing the ground motion components at both ends of the bridge. The displacement difference in each group is shown in the Figs. 20–21. Similar to the uniform excitation, the displacement and axial force responses of key nodes under non-uniform excitation are also given in Figs. 22–23 and Tables 11–12.

Table 11
Displacement response of key nodes under non-uniform excitation

Position		No.1 Arch rib								
		2			3			4		
Result		Axial direction	Transverse direction	Vertical direction	Axial direction	Transverse direction	Vertical direction	Axial direction	Transverse direction	Vertical direction
306–307	Finite element	15.90	67.12	13.91	20.58	84.05	16.74	17.75	74.45	15.85
	Experiment	15.03	79.07	14.64	22.73	88.06	17.90	16.09	87.21	12.94
	Relative error	5.80%	15.11%	4.98%	9.46%	4.55%	6.45%	10.33%	14.63%	22.51%
306–308	Finite element	15.52	69.34	13.23	19.49	79.67	15.28	14.66	72.11	14.64
	Experiment	17.33	70.47	12.74	19.75	94.79	14.41	13.00	82.88	17.26
	Relative error	10.46%	1.61%	3.87%	1.31%	15.95%	6.04%	12.75%	13.00%	15.17%

Table 12
Axial force response of key nodes under non-uniform excitation

Position		No.1 Arch rib					No.2 Arch rib				
		1	2	3	4	5	1	2	3	4	5
306–307	Finite element	9562.56	3709.67	2417.86	2727.17	8117.63	8954.65	3096.37	2498.82	3094.64	8523.53
	Experiment	10595.42	3565.77	2712.47	3502.67	9624.04	9716.56	2983.09	2670.42	2560.19	10700.87
	Relative error	9.75%	4.04%	10.86%	22.14%	15.65%	7.84%	3.80%	6.43%	20.88%	20.35%
306–308	Finite element	9484.03	3784.69	2630.52	3264.96	8432.01	9656.67	3569.17	2577.93	3068.03	8782.99
	Experiment	8608.14	3320.77	2761.13	2965.10	9876.78	8479.20	3122.36	2379.12	2548.18	10101.46
	Relative error	10.18%	13.97%	4.73%	10.11%	14.63%	13.89%	14.31%	8.36%	20.40%	13.05%

From the above seismic response data, the following conclusions can be drawn. 1. The damage state of bridge can be controlled within the range of slight damage, the maximum displacement of arch rib is 94.79mm, and the maximum axial force is 10700kN. Compared with the results in uniform excitation, the maximum displacement decreases by 19mm and the axial force increases by 2235kN. 2. The non-uniform excitation can significantly increase the internal force response of arch rib. Under 306–307 and 306–308 working conditions, the average peak displacement of key nodes is 37.78mm and 36.48mm, and the average peak axial force is 5566.72kN and 5470.66kN, respectively. From the

average peak displacement, the results of uniform excitation and non-uniform excitation are similar, and the displacement response of non-uniform excitation increases by 11.89%. The peak value of the average axial force of the key joints of arch rib under non-uniform excitation is 5518.69kN, which is 63.97% higher than that of uniform excitation. 3. The seismic response of the arch rib is related to the relative displacement between the two earthquakes under non-uniform excitation. The larger the displacement difference, the greater the displacement and axial force response of arch rib. The maximum moment of displacement and axial force response of arch rib is consistent with the maximum moment of relative displacement difference of excitation, which is in 9s to 10s. 4. The relative difference of uniform excitation is basically consistent with that of non-uniform excitation. The test system can measure the seismic response of non-uniform excitation stably, and the difference does not obviously change.

Conclusion

The purpose of this paper is to study the influence of strong spatially varying of near fault earthquakes on long-span and large stiffness bridges. Taking a steel box arch bridge as an engineering case, the ground motion records collected in the near fault area are used as input, and the shaking table experiment and finite element analysis are used to analyze the entire process of seismic damage. Based on the analysis of the internal force and displacement seismic response of some key positions, the following conclusions can be obtained.

1. No matter under uniform excitation or non-uniform excitation, the seismic damage of the bridge can be controlled in the range of slight damage, and there will be no serious damage or collapse. Under the two conditions, the maximum displacement of vault can be controlled less than 113.8mm, and the maximum axial force of arch foot can be controlled less than 10700kN. 2. Under the non-uniform excitation, the internal force response of the key nodes of the arch rib increases significantly, while the displacement response is basically consistent with the uniform excitation. The peak value of average axial force of key nodes of arch rib under non-uniform excitation is 5518.69kN, which is 63.97% higher than that under uniform excitation. 3. For non-uniform excitation, the seismic response of arch rib is greatly affected by the relative displacement between two ground motion excitations. Based on the above conclusions, the spatially varying in the near fault area is very significant. If this strong spatially varying is ignored, the structural damage in the near fault region is likely to be underestimated.

Declarations

Acknowledgments

This work is supported by the National Natural Science Foundation Key Project of China (No. 51178080) and Doctoral Research Initiation Fund of Shandong Technology and Business University (No. BS201931). The author would like to thank the Pacific Earthquake Engineering Research (PEER) Center for the earthquake data.

Author information

Shandong technology and business University, China

Zhen Liu &, Shibo Zhang

Corresponding author

Correspondence to Zhen Liu

References

1. Abdollahzadeh, G., Hadi F., and Hedieh E.. (2018). Comparing Hysteretic Energy and inter-story drift in steel frames with V-shaped brace under near and far fault earthquakes. *Alexandria Engineering Journal*, **57**(1), 301-308. <https://doi.org/10.1016/j.aej.2016.09.015>
2. Adanur S, Altunişik A C, Soyuluk K, *et al*(2016) Multiple-support seismic response of bosphorus suspension bridge for various random vibration methods. *Case Studies in Structural Engineering* **5**: 54-67. <https://doi.org/10.1016/j.csse.2016.04.001>
3. Cao Y, Mavroeidis G P, Meza-Fajardo K C, *et al*. (2017) Accidental eccentricity in symmetric buildings due to wave passage effects arising from near-fault pulse-like ground motions. *Earthquake Engineering & Structural Dynamics* **46**(13): 2185-2207. <https://doi.org/10.1002/eqe.2901>
4. Dinh, V.-N., Biswajit B., and Ronald B J B..(2014) Wavelet-based evolutionary response of multispan structures including wave-passage and site-response effects. *Journal of Engineering Mechanics* **140**(8): 04014056. [https://doi.org/10.1061/\(ASCE\)EM.1943-7889.0000708](https://doi.org/10.1061/(ASCE)EM.1943-7889.0000708)
5. Ellsworth W L, Celebi M, Evans J R, *et al* (2004) Near-field ground motion of the 2002 Denali Fault, Alaska, earthquake recorded at Pump Station 10. *Earthquake Spectra* **20**(3): 597-615. <http://dx.doi.org/10.1193/1.1778172>

6. Fang C, Zhong Q, Wang W, *et al.* (2018): Peak and residual responses of steel moment-resisting and braced frames under pulse-like near-fault earthquakes. *Engineering Structures* **177**: 579-597. <https://doi.org/10.1016/j.engstruct.2018.10.013>
7. Goel, R. K., and Anil K. C..(2008) Role of shear keys in seismic behavior of bridges crossing fault-rupture zones. *Journal of Bridge Engineering* **13**(4): 398-408. [https://doi.org/10.1061/\(ASCE\)1084-0702\(2008\)13:4\(398\)](https://doi.org/10.1061/(ASCE)1084-0702(2008)13:4(398))
8. Goel R, Qu B, Tures J, *et al.*(2014) Validation of fault rupture-response spectrum analysis method for curved bridges crossing strike-slip fault rupture zones. *Journal of Bridge Engineering* **19**(5): 06014002. [https://doi.org/10.1061/\(ASCE\)BE.1943-5592.0000602](https://doi.org/10.1061/(ASCE)BE.1943-5592.0000602)
9. Guo W, Gao X, Hu P, *et al.*(2020) Seismic damage features of high-speed railway simply supported bridge-track system under near-fault earthquake. *Advances in Structural Engineering*, **23**(8): 1573-1586. <https://doi.org/10.1177/1369433219896166>
10. Konakli, K., and Armen D.K.. (2012) Simulation of spatially varying ground motions including incoherence, wave-passage and differential site-response effects. *Earthquake Engineering & Structural Dynamics* **41**(3): 495-513. <https://doi.org/10.1002/eqe.1141>
11. Mehanny, S. S. F., Ramadan O. M. O., and Howary.H. A. El (2014) Assessment of bridge vulnerability due to seismic excitations considering wave passage effects. *Engineering Structures* **70**: 197-207. <https://doi.org/10.1016/j.engstruct.2014.04.010>
12. Pan, X., Zheng, Z. & Wang, Z(2017). Amplification factors for design of nonstructural components considering the near-fault pulse-like ground motions. *Bull Earthquake Eng* **15**, 1519–1541. <https://doi.org/10.1007/s10518-016-0031-4>
13. Wilson, J. C.(2003) Repair of new long-span bridges damaged by the 1995 Kobe earthquake. *Journal of Performance of Constructed Facilities* **17**(4): 196-205. [https://doi.org/10.1061/\(ASCE\)0887-3828\(2003\)17:4\(196\)](https://doi.org/10.1061/(ASCE)0887-3828(2003)17:4(196))
14. Zhao, J.J..(2014) Large-Span Cable-Stayed Bridge Seismic Response Analysis Considering Traveling Wave Effect. *Applied Mechanics and Materials*. **477-477**: 1034-1037. <https://doi.org/10.4028/www.scientific.net/AMM.477-478.1034>
15. Zhang, C. *et al.* (2020). Influence of near-fault ground motion characteristics on the seismic response of cable-stayed bridges. *Bull Earthquake Eng* **18**, 6375–6403 <https://doi.org/10.1007/s10518-020-00926-9>
16. Zhong, J., *et al.* (2020) Near-fault seismic risk assessment of simply supported bridges. *Earthquake Spectra* **36**.4: 1645-1669. <https://doi.org/10.1177/8755293020935145>

Figures

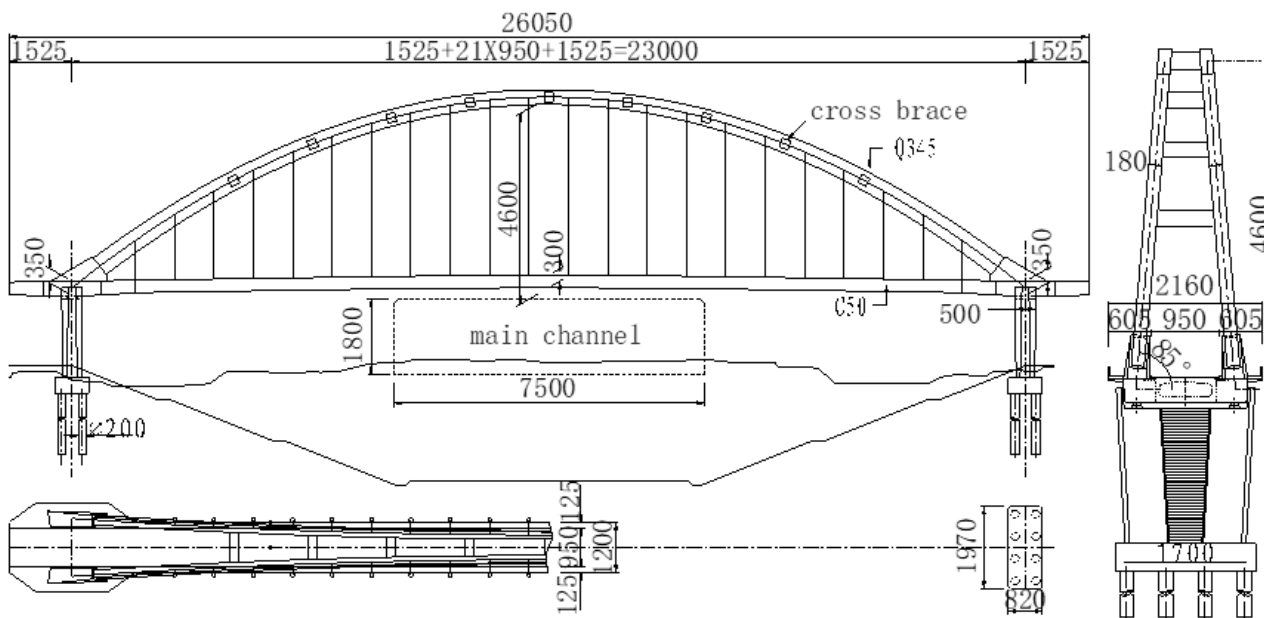


Figure 1

The overview of bridge unit

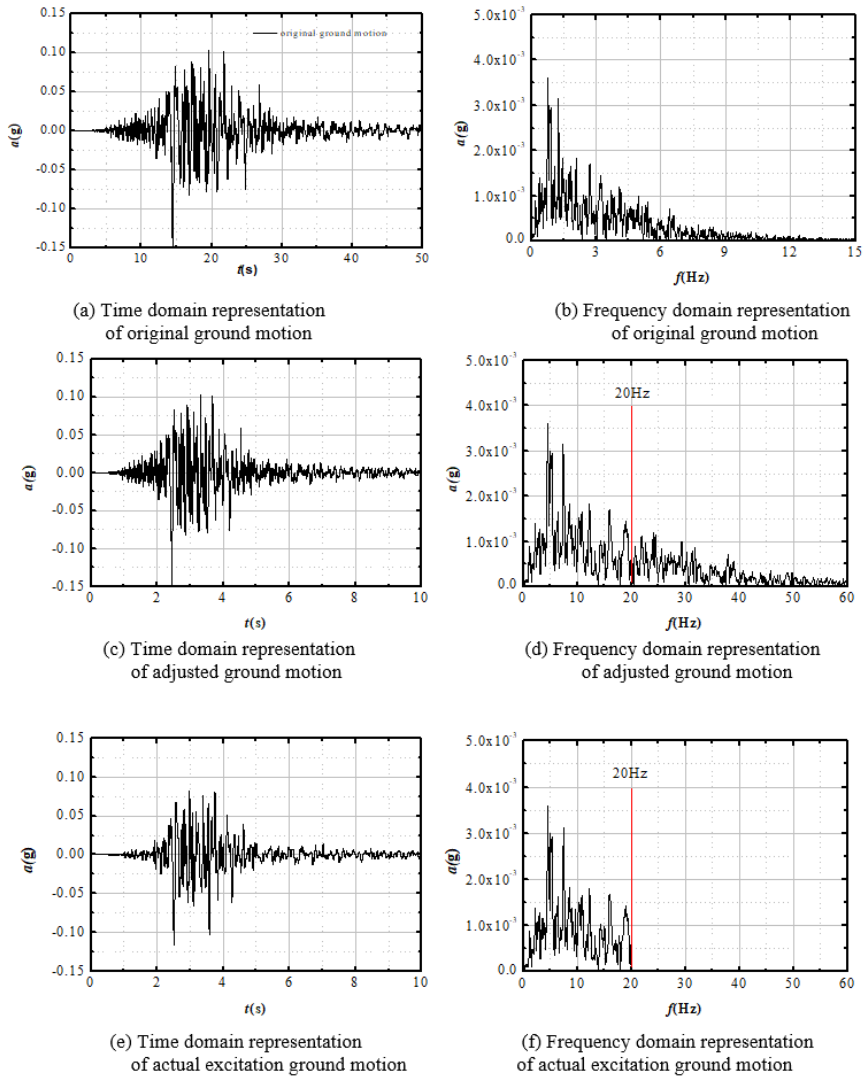


Figure 2

Acceleration time history of ground motion

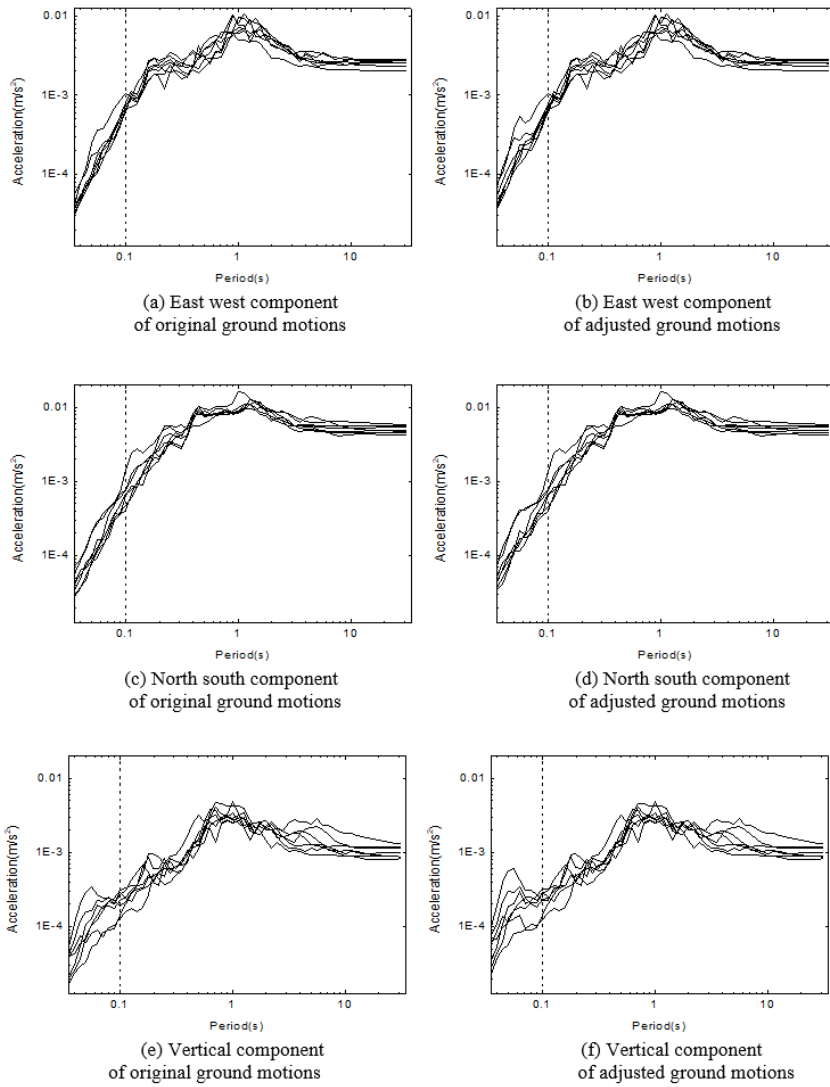


Figure 3

Acceleration response spectra of ground motion

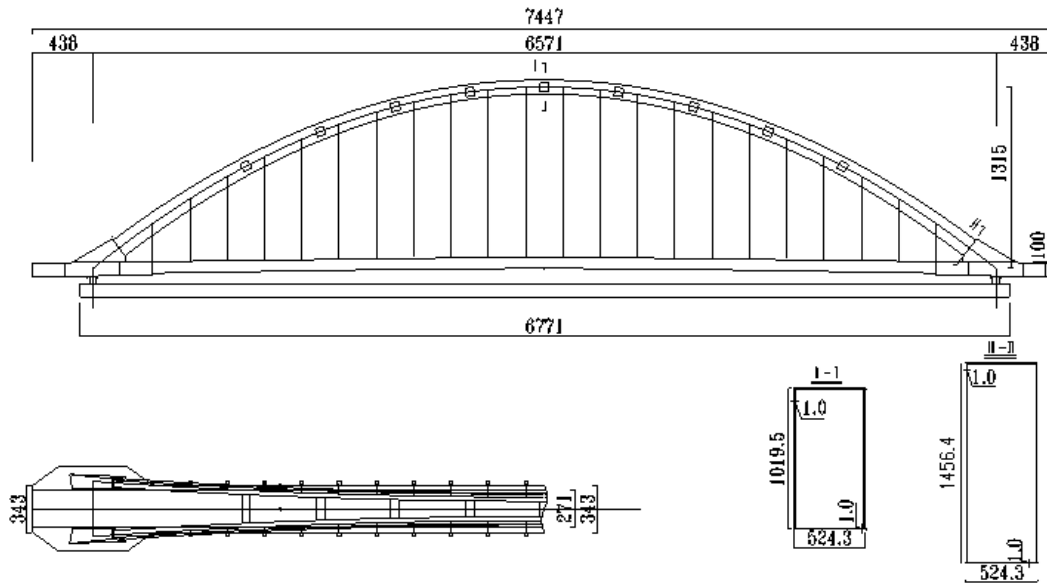


Figure 4

Size of scaled model(unit: mm)

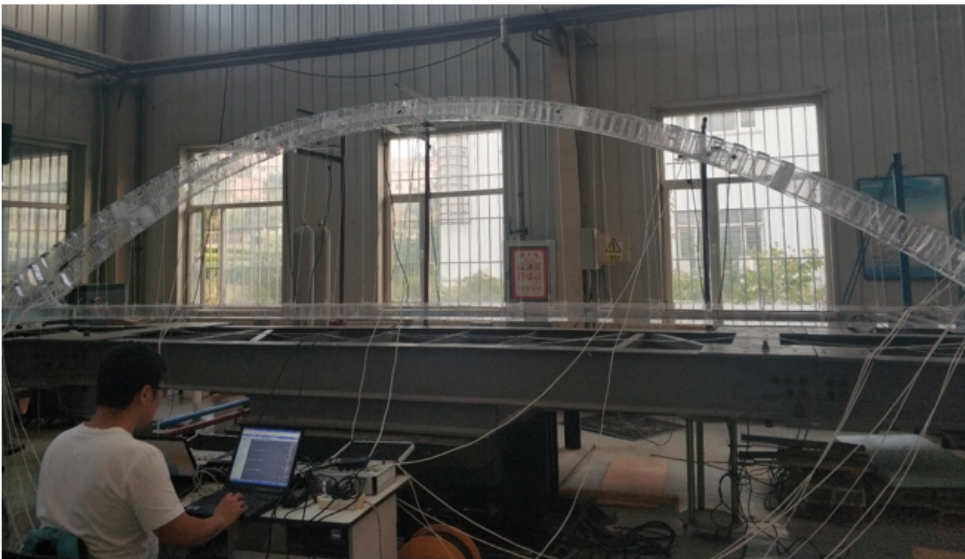


Figure 5

Bridge model

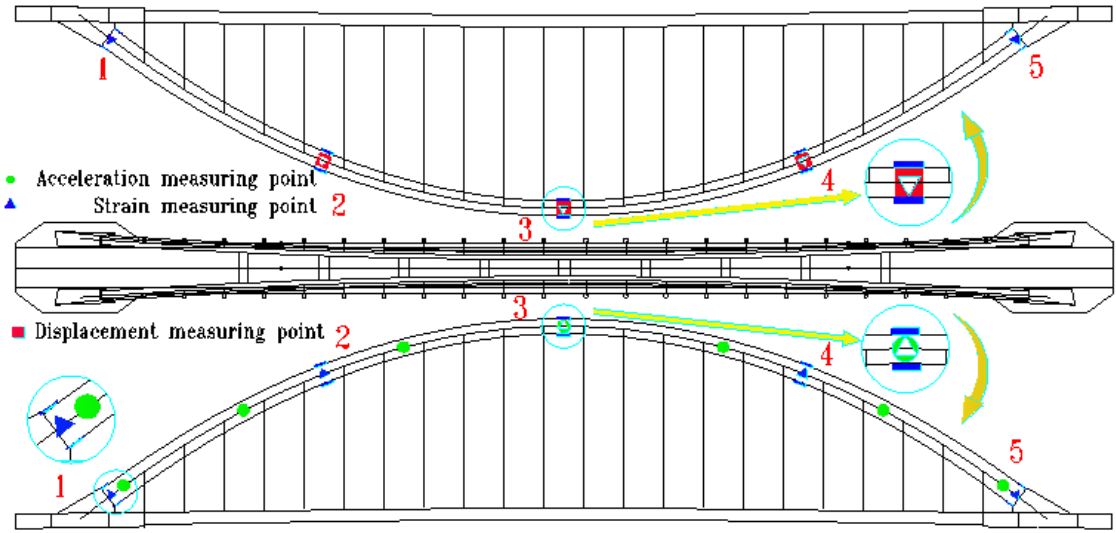


Figure 6

Arrangement of measuring points



Figure 7

Data acquisition system

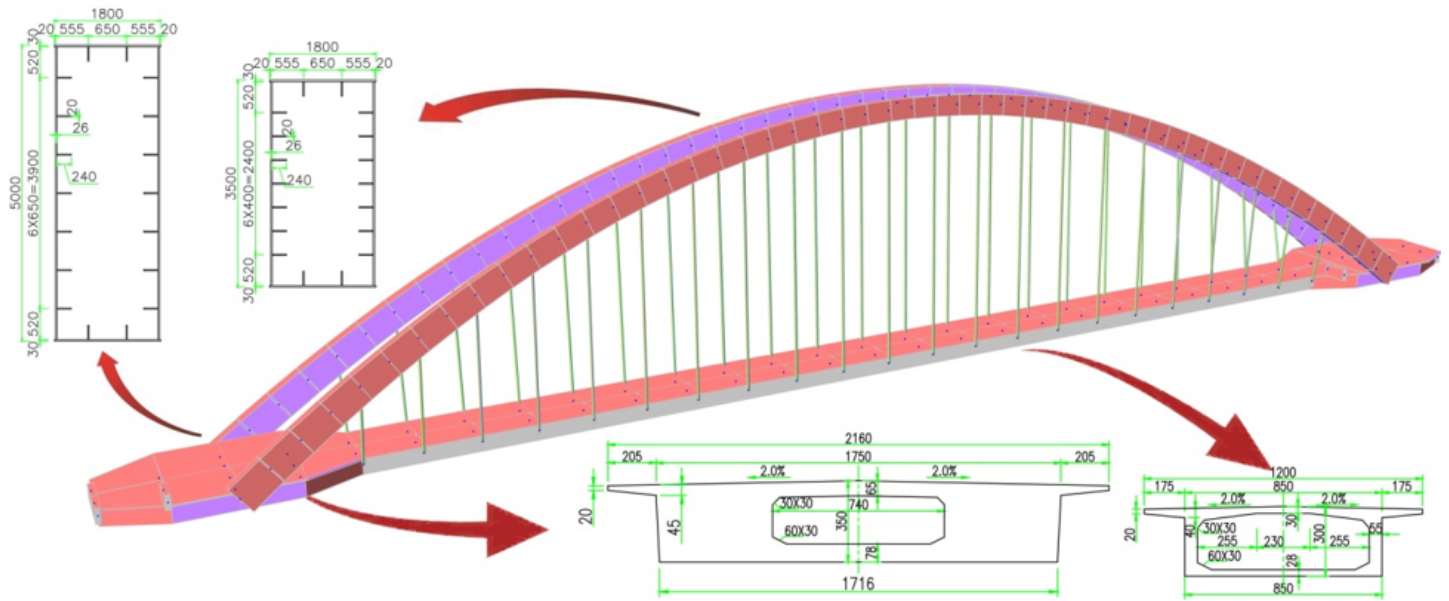


Figure 8

Finite element model of bridge case

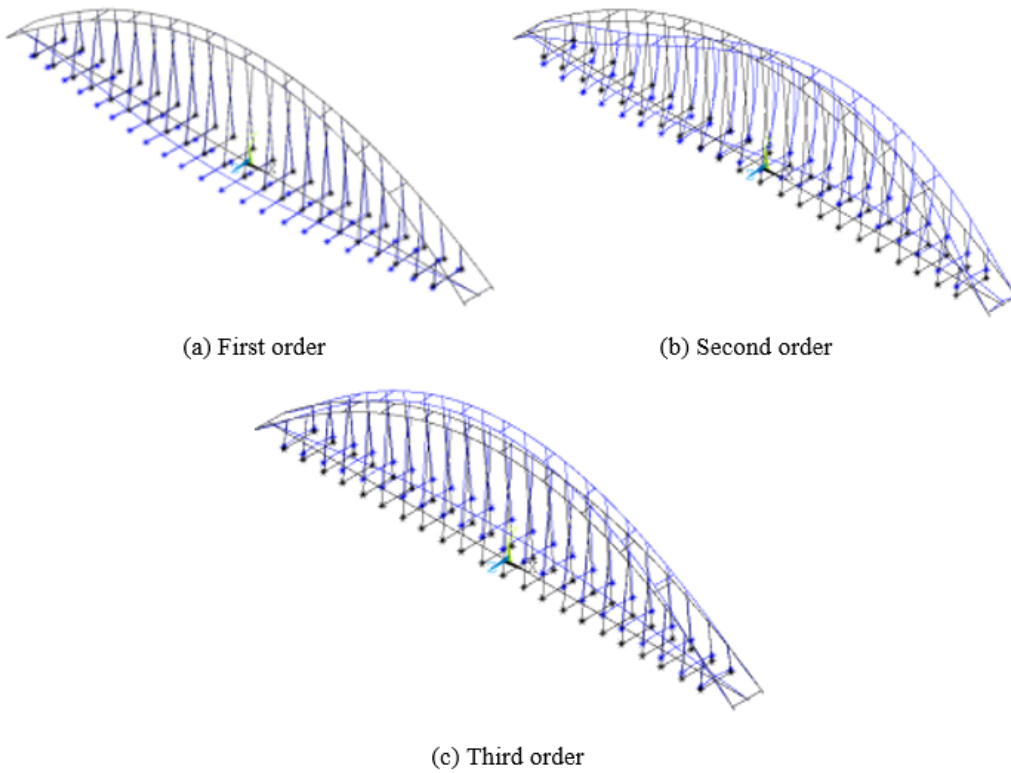


Figure 9

Vibration modes of finite element model

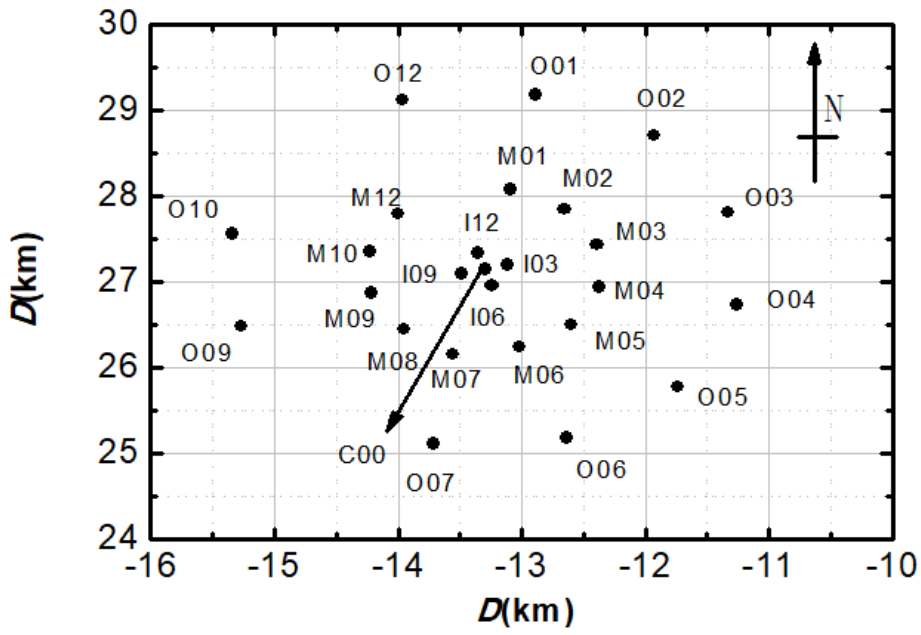


Figure 10

Sample coordinates of ground motion

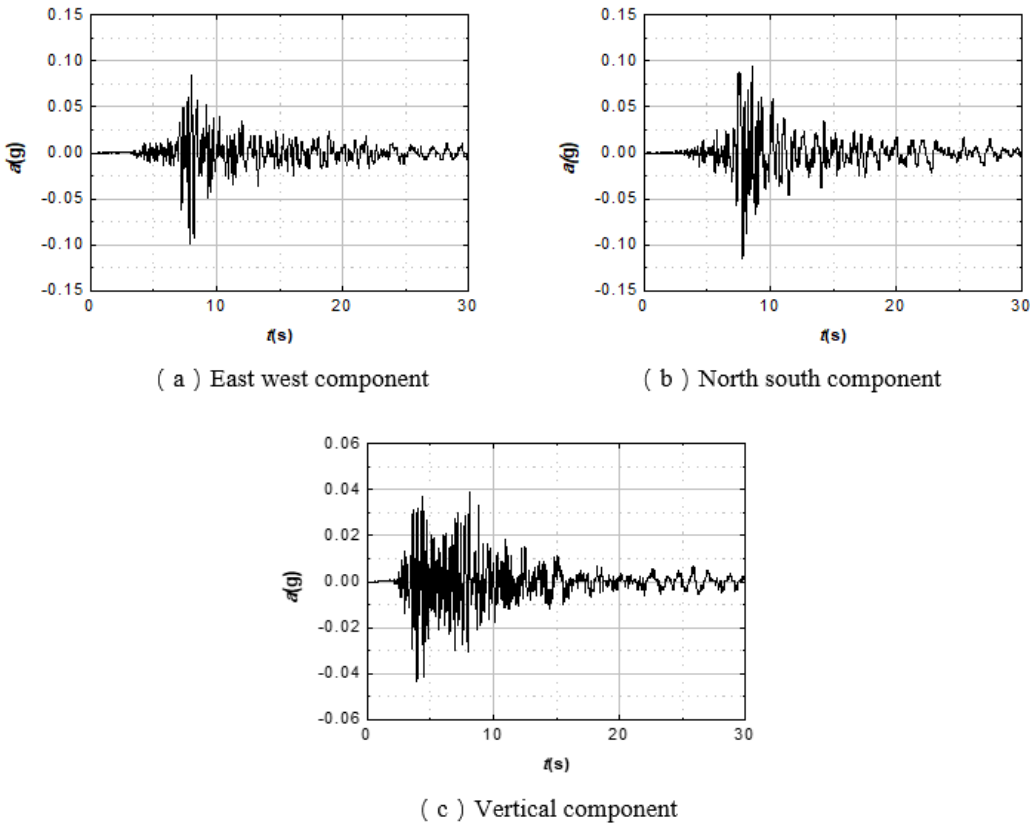
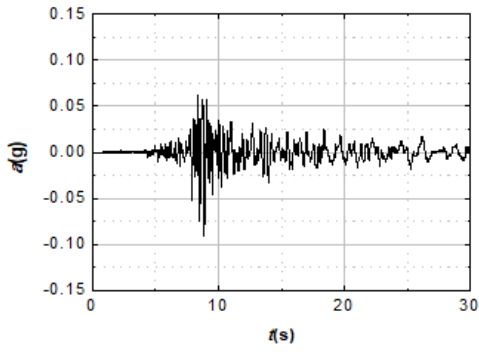
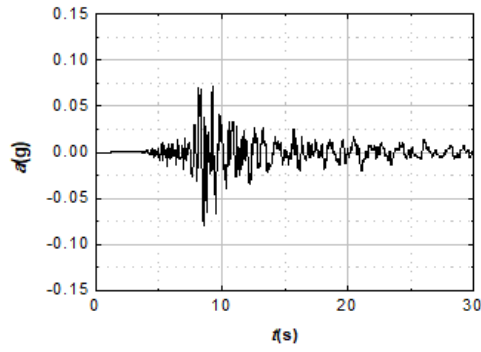


Figure 11

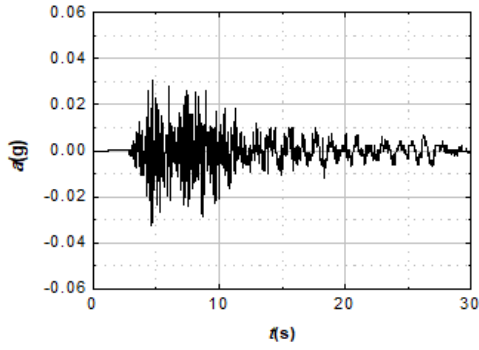
Acceleration time history of No.306 ground motions



(a) East west component



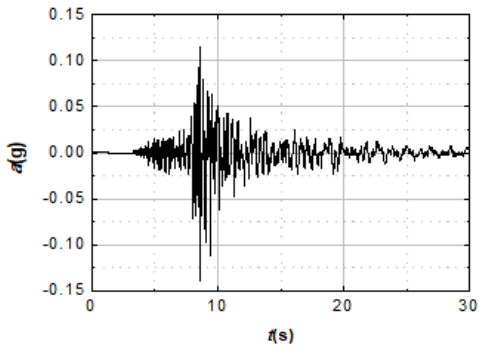
(b) North south component



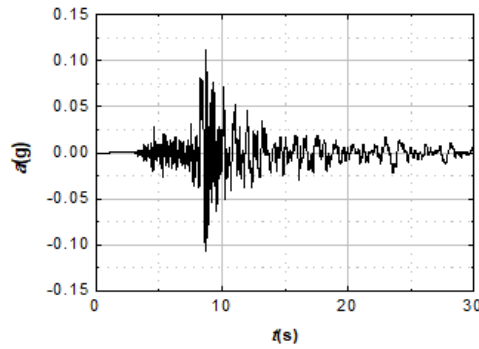
(c) Vertical component

Figure 12

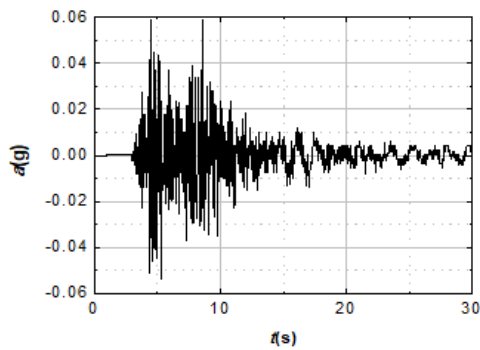
Acceleration time history of No.307 ground motions



(a) East west component



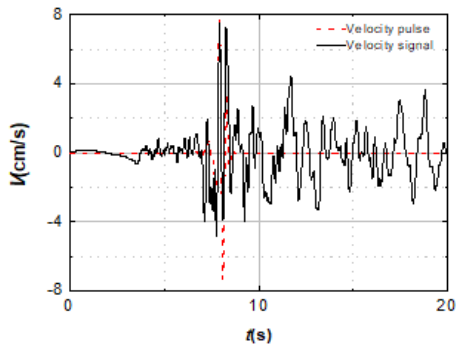
(b) North south component



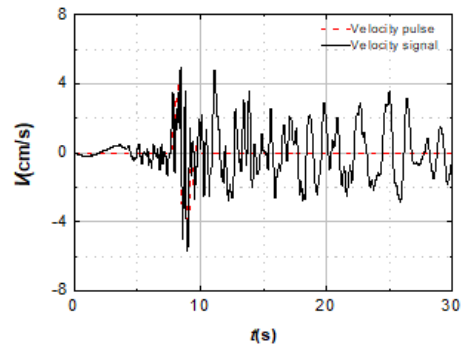
(c) Vertical component

Figure 13

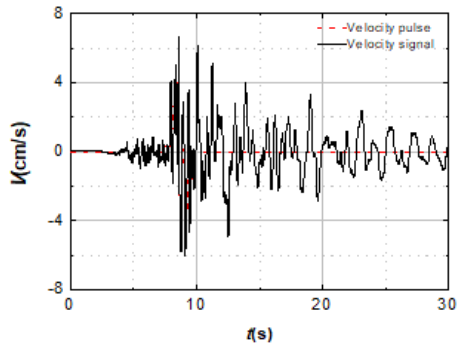
Acceleration time history of No.308 ground motions



(a) No.306 ground motions



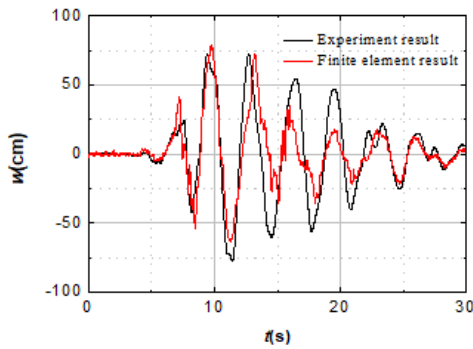
(b) No.307 ground motions



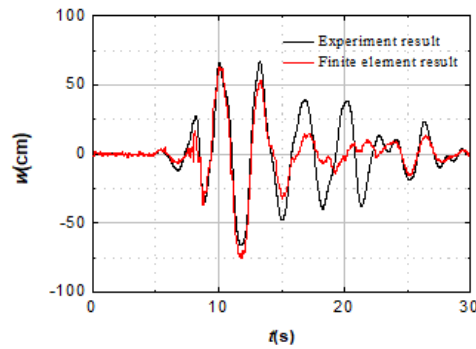
(c) No.308 ground motions

Figure 14

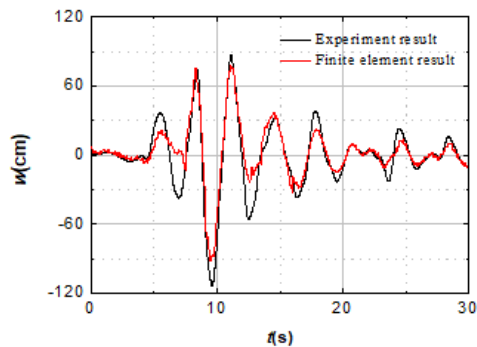
Velocity pulse extraction



(a) No.306 ground motions



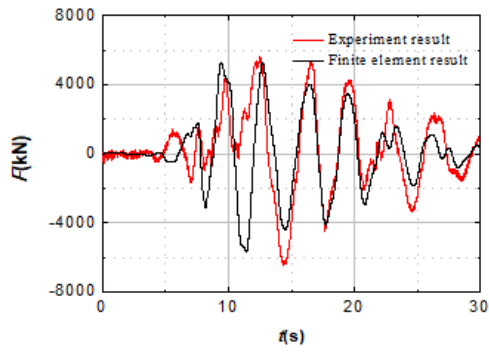
(b) No.307 ground motions



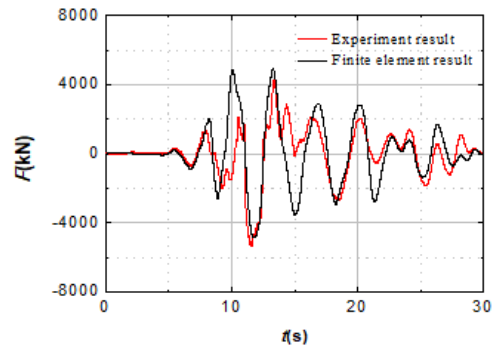
(c) No.308 ground motions

Figure 15

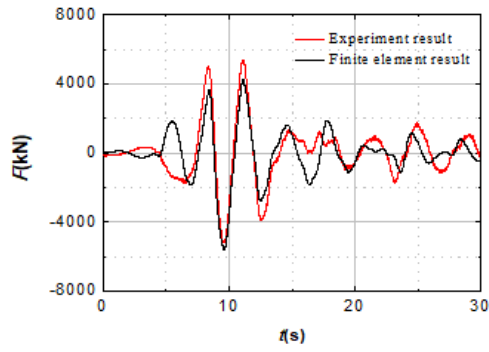
Transverse displacement time history of arch rib top



(a) No.306 ground motions



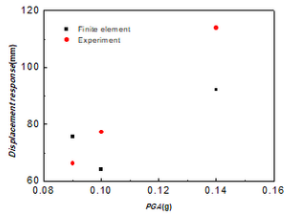
(b) No.307 ground motions



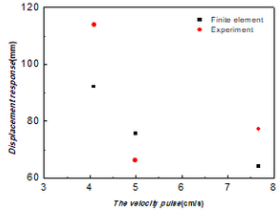
(c) No.308 ground motions

Figure 16

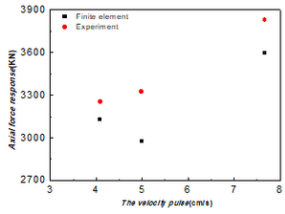
Time history of axial internal force of arch foot



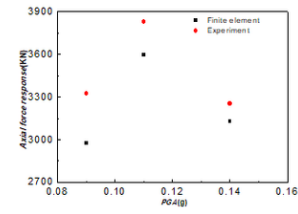
(a) Relationship between the maximum transverse displacement of the arch crown and the maximum acceleration of transverse ground motion excitation



(b) Relationship between the maximum transverse displacement of the arch crown and peak value of ground motion velocity pulse



(c) Relationship between the average axial force of key nodes of the arch rib and peak value of ground motion velocity pulse



(d) Relationship between the average axial force of key nodes of the arch rib and the maximum peak acceleration of ground motion excitation

Figure 17

Correlation between key seismic response and ground motion excitation

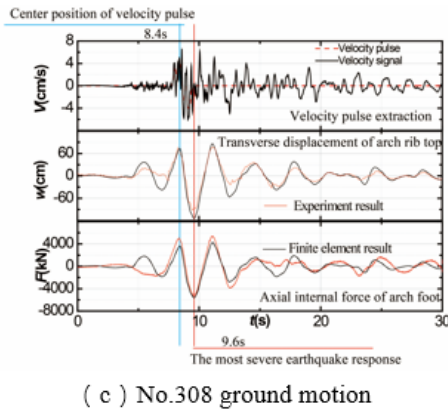
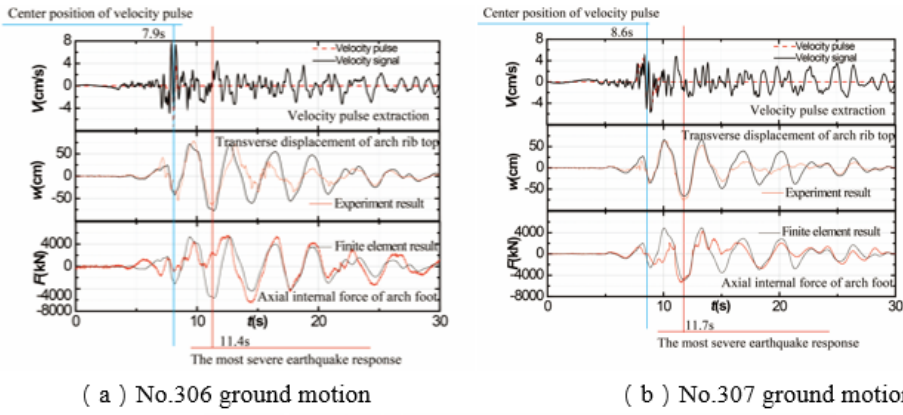


Figure 18

Comparison of ground motion excitation and seismic response of key nodes

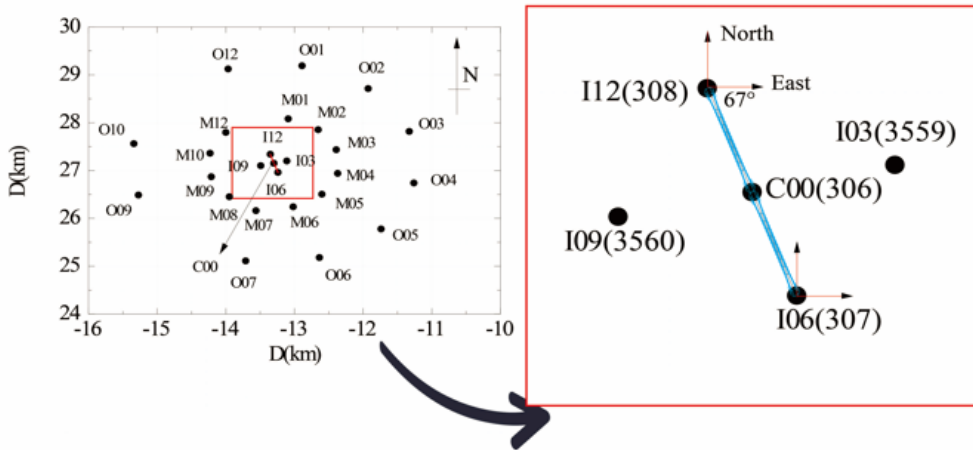
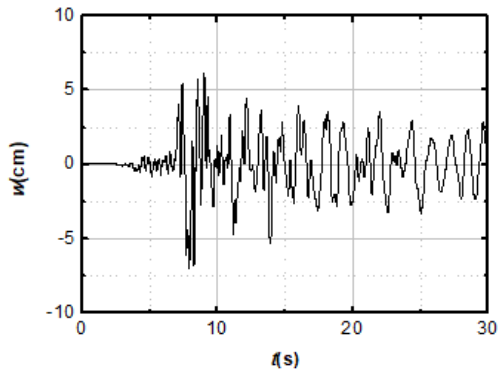
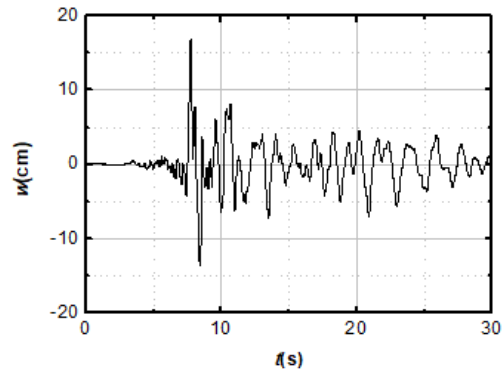


Figure 19

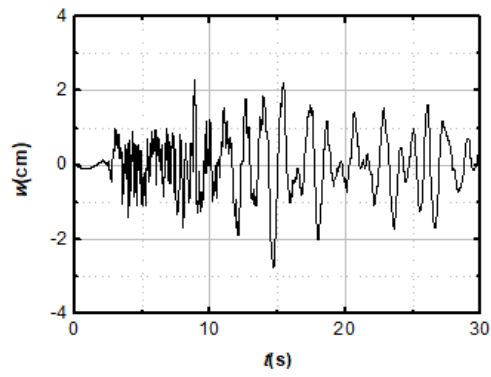
Schematic diagram of input direction of ground motion excitation



(a) longitudinal bridge component



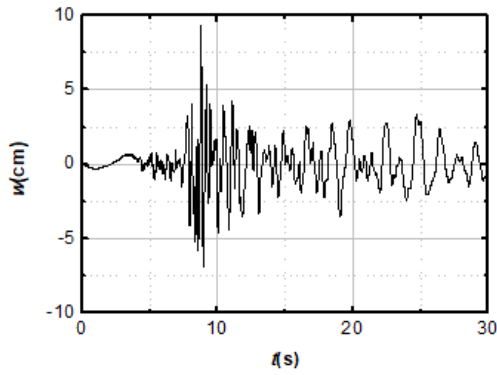
(b) transverse bridge component



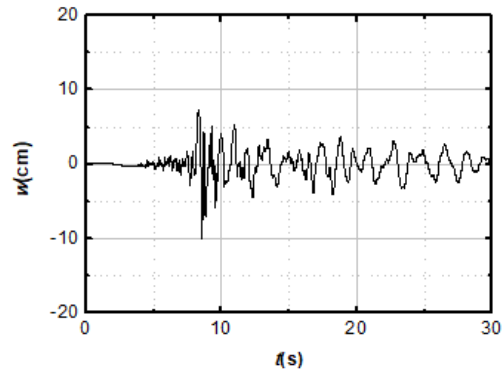
(c) Vertical component

Figure 20

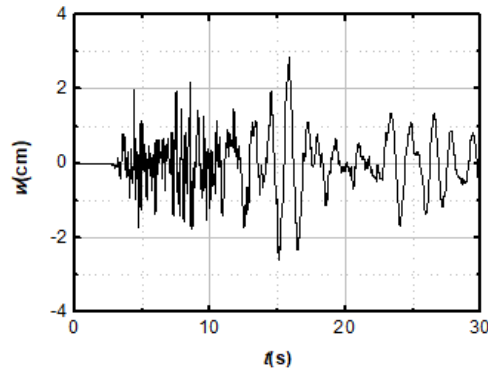
Relative motion between ground motions 306 and 307 under non-uniform excitation



(a) longitudinal bridge component



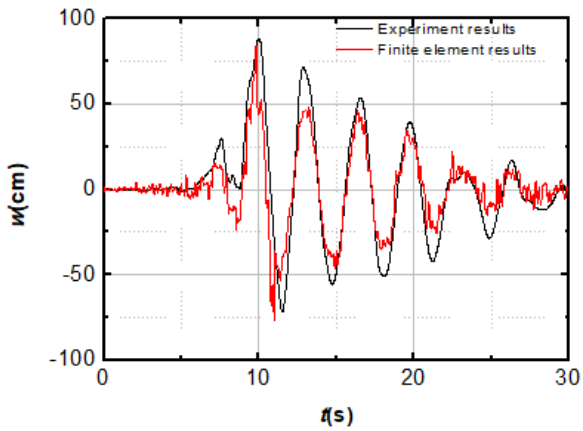
(b) transverse bridge component



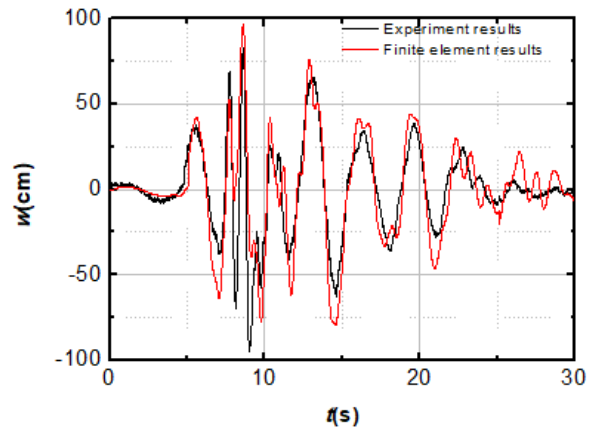
(c) Vertical component

Figure 21

Relative motion between ground motions 307 and 308 under non-uniform excitation



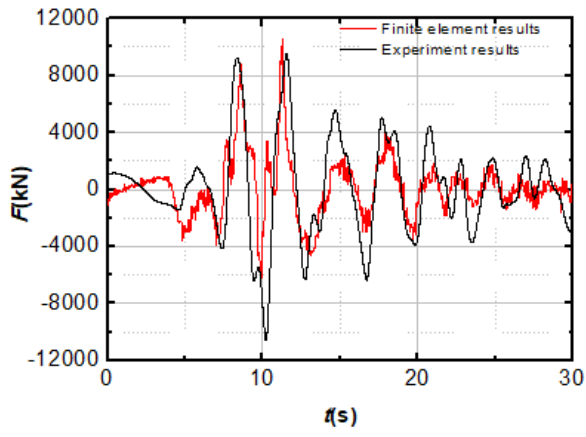
(a) No. 306-307 ground motions



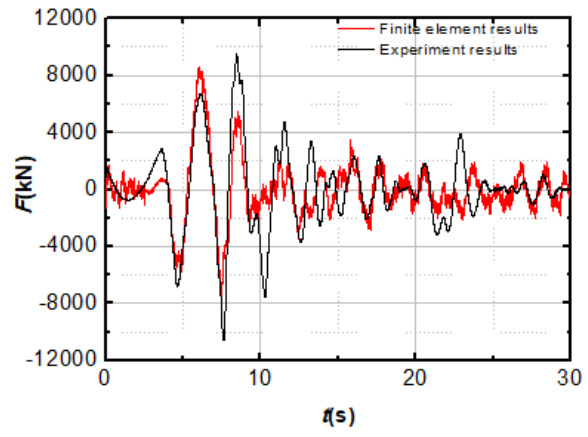
(b) No. 306-308 ground motions

Figure 22

Transverse displacement time history of arch rib top under non-uniform excitation



(a) No. 306-307 ground motions



(b) No. 306-308 ground motions

Figure 23

Time history of axial internal force of arch foot under non-uniform excitation